PNAS RESEARCH ARTICLE | EARTH, ATMOSPHERIC, AND PLANETARY SCIENCES OPEN ACCESS

Sunlight can convert atmospheric aerosols into a glassy solid state and modify their environmental impacts

Vahe J. Baboomian[a,1], Giuseppe V. Crescenzo[b,1], Yuanzhou Huang[b,2], Fabian Mahrt[b,c], Manabu Shiraiwa[a], Allan K. Bertram[b,3], and Sergey A. Nizkorodov[a,3]

Edited by Margaret Tolbert, University of Colorado, Boulder, Boulder, CO; received May 10, 2022; accepted August 24, 2022

Secondary organic aerosol (SOA) plays a critical, yet uncertain, role in air quality and climate. Once formed, SOA is transported throughout the atmosphere and is exposed to solar UV light. Information on the viscosity of SOA, and how it may change with solar UV exposure, is needed to accurately predict air quality and climate. However, the effect of solar UV radiation on the viscosity of SOA and the associated implications for air quality and climate predictions is largely unknown. Here, we report the viscosity of SOA after exposure to UV radiation, equivalent to a UV exposure of 6 to 14 d at midlatitudes in summer. Surprisingly, UV-aging led to as much as five orders of magnitude increase in viscosity compared to unirradiated SOA. This increase in viscosity can be rationalized in part by an increase in molecular mass and oxidation of organic molecules constituting the SOA material, as determined by high-resolution mass spectrometry. We demonstrate that UV-aging can lead to an increased abundance of aerosols in the atmosphere in a glassy solid state. Therefore, UV-aging could represent an unrecognized source of nuclei for ice clouds in the atmosphere, with important implications for Earth's energy budget. We also show that UV-aging increases the mixing times within SOA particles by up to five orders of magnitude throughout the troposphere with important implications for predicting the growth, evaporation, and size distribution of SOA, and hence, air pollution and climate.

secondary organic aerosol | condensed-phase photochemistry | particle viscosity | particle mixing time | atmospheric chemistry

Significance

Secondary organic aerosol is well known to affect Earth's climate, regional weather, visibility, and public health. Once these aerosols are formed, they are transported throughout the atmosphere for days or even weeks. We show that exposure of secondary organic aerosols to UV solar radiation leads to a surprising and remarkable increase in viscosity by as much as five orders of magnitude. We also show that this UV exposure can lead to an increased abundance of aerosols that are in the glassy solid state in the troposphere, with important implications for climate predictions. Overall, our results clearly demonstrate that aging by exposure to solar radiation needs to be considered when predicting the environmental impacts of secondary organic aerosols.

Secondary organic aerosol (SOA) represents a considerable mass fraction of atmospheric aerosol particles. SOA can directly affect climate by scattering shortwave radiation, or indirectly by acting as nuclei for cloud droplets and ice crystals (1–4). SOA also contributes to poor air quality in urban areas (5–9).

SOA is often formed through the oxidation of anthropogenic and biogenic volatile organic compounds (VOCs), followed by gas-particle partitioning of the semivolatile and low-volatility oxidation products (10–12). Of the total mass of global VOCs, ~90% originates from biogenic sources, with monoterpenes (C_{10}) being one of the most important types of biogenic VOCs (4, 10–12).

Once formed in the atmosphere, SOA is transported throughout the troposphere (13–15). SOA has average lifetimes on the order of 1 to 2 wk (14,16), but can be considerably longer in the upper troposphere. During this atmospheric transport, SOA particles can undergo aging by multiple processes, including heterogeneous oxidation (17–19), aqueous phase photooxidation (20–23), photosensitized uptake of gases (24–27), and UV-aging (28–33). Aging processes can change the physicochemical properties of aerosols. For example, UV-aging was reported to decrease mass, increase the oxidation state, decrease the volatility, and decrease the light absorption and scattering ability of SOA particles (24, 28, 31, 34–37).

To predict the importance of SOA for air pollution and climate, information on viscosity and diffusion rates within SOA particles is needed (38). Viscosity and diffusivity are inversely related as described with the Stokes-Einstein equation. Slower diffusion rates have been found to affect gas-particle partitioning and hence the evolution of mass and size distributions of SOA (39, 40). Molecular diffusion also affects rates and mechanisms of multiphase reactions within SOA, which in turn dictate SOA composition (41, 42) and long-range transport of pollutants such as polycyclic aromatic hydrocarbons (43–47). Viscous aerosols have been shown to create anoxic conditions as well as limit molecular motion, resulting in the stabilization of photochemically produced radicals, trapping them in the organic matrix (48, 49). Furthermore, the viscosity of SOA can impact their ability to act as cloud condensation nuclei (50) and ice nuclei (51). For example, if SOA particles are in a glassy solid state, defined as a material with a viscosity greater than 10^{12} Pa s, they may act as heterogeneous ice nuclei in clouds (14, 52, 53).

Author affiliations: [a]Department of Chemistry, University of California, Irvine, CA 92697; [b]Department of Chemistry, University of British Columbia, Vancouver, BC V6T1Z1, Canada; and [c]Laboratory of Environmental Chemistry, Paul Scherrer Institute, 5232 Villigen, Switzerland

Author contributions: V.J.B., G.V.C., M.S., A.K.B., and S.A.N. designed research; V.J.B., G.V.C., Y.H., and F.M. performed research; V.J.B., G.V.C., Y.H., and F.M. analyzed data; and V.J.B., G.V.C., Y.H., F.M., M.S., A.K.B., and S.A.N. wrote the paper.

The authors declare no competing interest.

This article is a PNAS Direct Submission.

[1]V.J.B. and G.V.C. contributed equally to this work.

[2]Present address: Anton Paar Canada Inc., H4R 2Z8, Saint Laurent, Canada.

[3]To whom correspondence may be addressed. Email: bertram@chem.ubc.ca or nizkorod@uci.edu.

This article contains supporting information online at http://www.pnas.org/lookup/suppl/doi:10.1073/pnas.2208121119/-/DCSupplemental.

Published October 21, 2022.

The viscosity of fresh, unaged SOA types has been reported in previous laboratory studies (54–58). In contrast, the viscosity of SOA material after aging has rarely been measured, and so far, no measurements of the SOA viscosity after UV exposure, hereafter referred to as UV-aging, have been reported. It is especially important to understand the effect of UV-aging on the viscosity of SOA in the upper troposphere, where particles can spend a long time interacting with solar radiation, and where the dry and low-temperature conditions in this part of the troposphere favor higher SOA viscosities. In addition to laboratory studies, recent modeling studies have used parameterizations based on viscosity measurements and glass transition temperatures to predict global distributions of viscosities and diffusion rates within SOA particles (40, 59–63). However, the effect of UV-aging on viscosity and diffusion rates within SOA was not explicitly considered in these studies. As a result, global distributions of viscosity and diffusion rates within SOA and associated atmospheric impacts remain highly uncertain.

To address these important gaps in knowledge, we measured the viscosity of SOA after exposure to UV radiation with a wavelength (λ) of 305 nm for 12 d and compared it to viscosity of control SOA samples that remained in darkness for the same period of time. This exposure time corresponds to an equivalent exposure of 6 to 14 d at midlatitudes during the summer (64, 65). We show that such UV-aging leads to considerable increases in viscosity and mixing times of organic molecules within a SOA particle by as much as five orders of magnitude compared to the unirradiated SOA particles. We show that these increases can be explained, at least in part, by an increase in average molecular mass and an increase in average elemental oxygen-to-carbon ratio of the organic molecules constituting the SOA material, as determined by high-resolution mass spectrometry. The increased viscosity of aged SOA likely leads to increased abundance of SOA in a glassy solid state that can potentially act as ice nucleating particles, with implications for climate predictions. We also show that mixing times within 200 nm SOA particles by molecular diffusion can often be larger than 0.5 h for most parts of the free troposphere, contrary to the assumptions frequently used in chemical transport models, with important implications for predicting the growth, evaporation, and size distribution of SOA, and hence, air pollution and climate.

Results

Viscosity of SOA With and Without UV-Aging. We measured the viscosity of SOA generated by 1) ozonolysis of d-limonene in an environmental chamber, 2) ozonolysis of d-limonene in a flow tube, and 3) ozonolysis of α-pinene in a flow tube (see *Materials and Methods* Section 1). Since α-pinene and d-limonene often dominate the atmospheric monoterpene emissions, they have been commonly used as representative monoterpenes in laboratory and modeling studies investigating SOA properties (4, 66–68). Aging by UV irradiation was achieved by placing a substrate with deposited SOA into a flow cell, where it was irradiated by a UV-light emitting diode (LED, centered at λ = 305 nm) while passing particle and VOC-free air continuously over it (see *Materials and Methods* Section 2). A control sample was prepared by exposing SOA to the same amount of particle and VOC-free air but without exposure to the UV radiation. The viscosity of control and aged SOA particles was determined using the poke-flow technique (see *Materials and Methods* Section 3). In the atmosphere, SOA particles will also be exposed to gas-phase oxidants (e.g., ozone and OH radicals), in addition to UV light, which can cause additional aging. Further studies are needed to determine if these gas-phase oxidants also cause changes in SOA viscosity. Our aging experiments were carried out in the absence of these gas-phase oxidants to isolate the effect of UV light.

Fig. 1*A* shows the viscosities for the control and aged SOA derived from d-limonene ozonolysis, produced in an environmental chamber. The viscosities were calculated from the flow times (*SI Appendix*, Fig. S1) observed during the poke-flow measurements. Our measured viscosities of control limonene SOA are similar to previous measurements with similar mass concentrations (*SI Appendix*, Fig. S4) (69–71), which suggests that our control samples are representative of fresh, unaged SOA. A striking and surprising result of our experiments shown in Fig. 1*A* is the increase in SOA particle viscosity by several orders of magnitude after UV exposure, across all relative humidity (RH) values investigated. For instance, under dry conditions, aging resulted in an increase in viscosity from 10^5 Pa s in the control d-limonene ozonolysis samples to at least 10^9 Pa s in the aged samples.

The same trend of increasing viscosity after UV exposure is observed for SOA generated from ozonolysis of d-limonene in a flow tube (Fig. 1b). The similar results for d-limonene generated

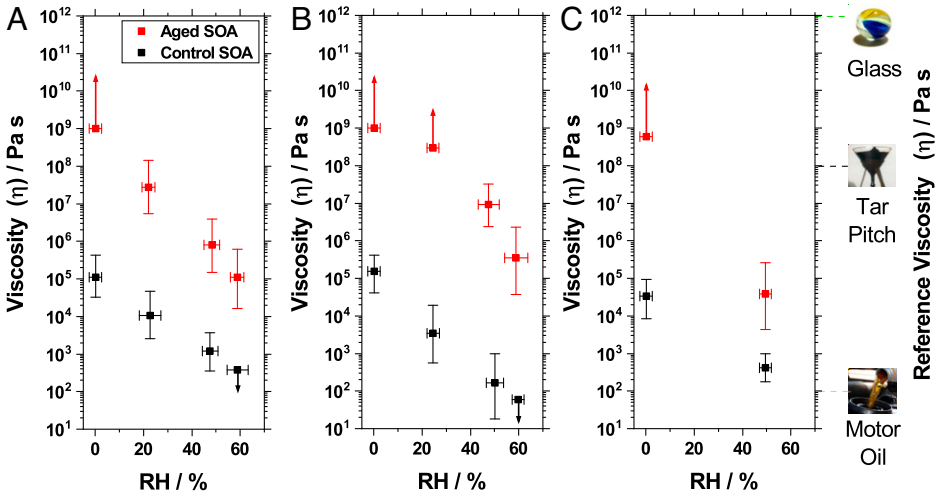

Fig. 1. Viscosities of control and aged SOA samples. Viscosity of SOA derived from ozonolysis of d-limonene and α-pinene measured at room temperature (292 K). Shown are viscosities of control (black squares) and aged by UV exposure (red squares) SOA particles. (*A*) d-limonene SOA produced in an environmental chamber, (*B*) d-limonene SOA produced in a flow tube, and (*C*) α-pinene SOA produced in a flow tube. Error bars in the y-direction correspond to the upper and lower limits of viscosities from the poke-flow experiments, error bars in the x-direction correspond to the uncertainty in the relative humidity through measurement of the dewpoint using a chilled mirror hygrometer. Upward arrows indicate lower viscosity limits, downward arrows indicate upper viscosity limits.

in an environmental chamber and flow tube with different ozone and SOA mass concentrations (see *Materials and Methods* Section 1 and *SI Appendix*, Table S1), suggests relatively low sensitivity of our results to ozone exposure and SOA mass concentrations.

An increase in viscosity driven by UV-aging was also observed for the SOA generated from ozonolysis of α-pinene in a flow tube (Fig. 1*C*). This shows that the effect of aging on viscosity is not unique to SOA from ozonolysis of d-limonene. Our measured viscosities of control α-pinene SOA are at the lower end of previous measurements for fresh SOA (*SI Appendix*, Fig. S5) (54, 72), and similar to predictions based on explicit modeling of gas-phase oxidation of α-pinene (73). The relative increase in viscosity after UV-aging is apparent in all of our measurements and is expected to occur for monoterpene derived SOA irrespective of the initial SOA viscosity.

Overall, the viscosity of all samples increased by four orders of magnitude after aging at 0% RH and upwards of two orders of magnitude at 50% RH (Fig. 1). Increasing the RH led to a decrease in the viscosity for both the control and aged SOA samples, due to water uptake into the particle phase (Fig. 1). This behavior is expected as water is known to act as a plasticizer that decreases the viscosity of the SOA material (28, 32, 57, 74).

Chemical Composition of SOA After UV-Aging. Fig. 2*A* shows the mass spectra of control and aged d-limonene SOA samples generated in an environmental chamber, as analyzed by liquid chromatography coupled to a high-resolution mass spectrometer (HRMS). All spectra were normalized to the sum of peak abundance in each sample. Spectra were collected in triplicates and only compounds present in all three independent runs were assigned to $C_xH_yO_z$ molecular formulas (see *Materials and Methods* Section 4). In our HRMS experiments, control samples had 1,003 assignable formulas, and aged samples had 1,428 assignable formulas including 673 assigned compounds that were unique to the aged SOA. Highlighted in Fig. 2*A* are the monomer, dimer, and trimer regions. Comparison of the mass spectra of control and aged SOA revealed that UV-aging led to a smoothing of the mass distribution of organic compounds. This is evident from the "filling-in" of the valleys between the more distinct monomer and the dimer regions visible in the control SOA spectrum, as well as between the dimer and trimer regions of the mass spectra shown in Fig. 2*A*.

This smoothing of the mass distribution is even more apparent in Fig. 2*B*, where the distribution of the number of carbon atoms per assigned compound is shown. Unlike the control samples, where the regions for monomer, dimer, and trimer appear as distinctly different modes, the distribution of the aged samples appear considerably more continuous. This smoothing corresponds to an increase in the average molecular weight from 245.6 g mol^{-1} to 270.3 g mol^{-1}, an increase of ∼10% (*SI Appendix*, Table S3).

Fig. 2*C* shows the double bond equivalent (DBE) as a function of the number of carbon atoms per assigned molecule (75). The aged SOA sample had compounds with increased DBE, particularly at higher molecular weights and carbon atom numbers, compared to compounds in the control SOA sample. This is in contrast to known reduction in DBE in photodegraded dissolved organic matter samples (76).

Overall, UV-aging of environmental chamber d-limonene SOA resulted in an average increase in molecular weight, elemental oxygen-to-carbon ratio (O:C), number of carbon atoms per molecule, and DBE by 10%, 12%, 6%, and 19%, respectively, while the hydrogen-to-carbon ratio (H:C) decreased by 5% (*SI Appendix*, Table S3). Similar changes in composition were also found in SOA particles generated by ozonolysis of d-limonene and α-pinene in a flow tube (see *SI Appendix*, Table S3 and Figs. S6 and S7). An increase in molecular weight, O:C ratio, and number of carbon atoms per molecule have previously all been correlated to an increase in particle viscosity (38, 77, 78). Hence, the increase in SOA particle viscosity resulting from UV exposure observed here is most likely due, at least in part, to changes in these chemical properties.

The smoothing of the distribution (Fig. 2 *A* and *B*) and the increase in the average molecular weight (*SI Appendix*, Table S3) are caused by the condensed-phase photochemical reactions occurring during the aging process. Previous studies have also found a smoother molecular weight distribution after UV-aging

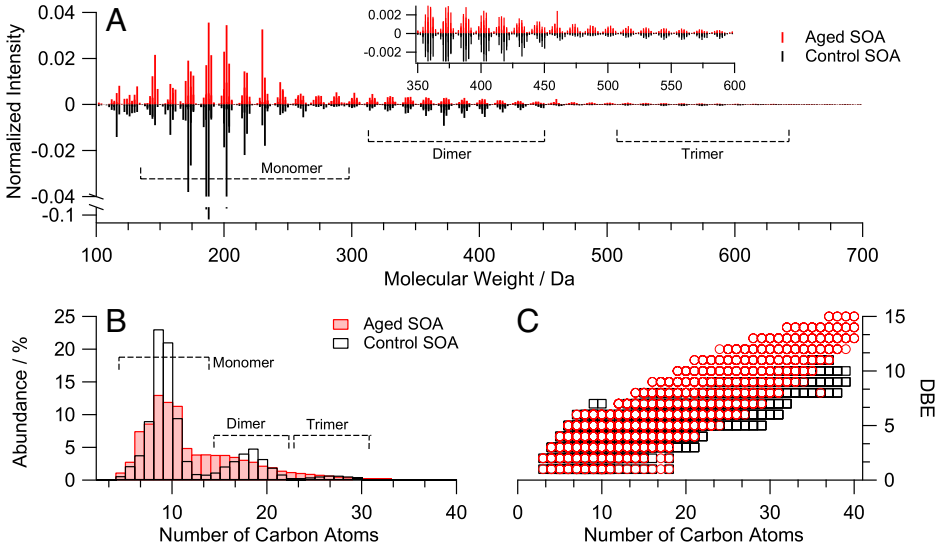

Fig. 2. Chemical composition of control and aged d-limonene ozonolysis SOA. HRMS results of SOA produced from d-limonene ozonolysis in an environmental chamber and changes in chemical composition due to UV-aging. Spectra were normalized to the sum of peak abundances per sample. (*A*) Mass spectra of the control and aged samples. The control sample spectrum has well-defined monomer, dimer, and trimer regions, indicated by the boxes, that are smoothed after UV-aging. A magnified view of the spectra above 350 Da is also shown. (*B*) Distribution of the number of carbon atoms per assigned compound that smooths in the aged samples. (*C*) DBE as a function of the number of carbon atoms in assigned molecules. The aged SOA compounds tend to have a higher DBE compared to the control sample.

of SOA (28, 29). Tropospheric UV irradiation (λ > 300 nm) has been shown to efficiently break carbonyl compounds through Norrish type-I and type-II reactions resulting in free radicals (30, 79, 80). The size of the radicals depends on the placement of the carbonyl group within the molecular skeleton. Because of the wide distribution of radical sizes and their secondary reactions, such as radical-radical recombination, they can produce a wider distribution of organic compounds, thus smoothing the distinction between the monomer and dimer compounds that is present in the control SOA material. The results in Fig. 2 *A* and *B* are consistent with a radical-radical recombination mechanism, with compounds unique to aged SOA appearing at higher carbon numbers. The smoother distribution may also be attributed to a Norrish photochemical mechanism (28, 29, 81), followed by the possible formation of carboxylic acid functional groups and subsequent dehydration and esterification reactions (29, 36, 82, 83).

The results shown in Fig. 2 and *SI Appendix*, Table S3 further highlight an interesting difference between photolytic studies of organic compounds in SOA samples at low relative humidities versus photolytic studies of SOA in dilute aqueous solutions, as in the latter the average molecular weight decreases and both dimers and trimers have been reported to become degraded (84, 85). While the underlying reason for this is still unknown, the difference could be due to changes in diffusion times of radicals that are produced during the UV exposure. Another possibility is the larger oxygen depletion in studies using SOA particles, compared to photolysis in dilute aqueous solutions. Additional studies are needed to better understand the specifics of the photochemical processes in different phases.

In our previous work, using similarly prepared SOA material, but using direct infusion instead of liquid chromatography HRMS, we did not observe an increase in molecular weight after UV-aging (28). The current study is more accurate in measuring relative ion abundances due to chromatographic separation reducing matrix effects that can occur with direct infusion (86–88). The current results are consistent with a recent study that observed an increase in average number of carbon atoms, O:C ratio, and DBE after UV-aging of SOA (29).

To link viscosity data (Fig. 1) to the molecular composition (Fig. 2), the HRMS data were used to predict viscosities, following the approach of DeRieux et al. (77). Following this approach, the assigned chemical formulas and abundances of the SOA compounds were used to predict the glass transition temperature, T_g, the temperature where the transition between the amorphous solid and semisolid phase states occurs (77, 89). Values of T_g of the SOA mixtures were derived using the Gordon-Taylor mixing rule and then converted to viscosity values using the Vogel-Tammann-Fulcher equation (*SI Appendix*, Section 2).

Fig. 3 shows a comparison of the experimentally measured viscosity values under dry conditions (filled circles) and those predicted by the parametrization (open squares). The predicted viscosities for the control SOA samples are 2 to 3 orders of magnitude higher than the measurements, depending on the SOA type. Nevertheless, a difference in predicted viscosities between control and aged samples is evident with a UV-induced increase in viscosity by 2 to 3 orders of magnitude. This further illustrates that the experimentally observed increases in viscosity is driven by the changes in chemical composition.

The predictions in Fig. 3 overestimate the viscosity for the control SOA and underestimate the difference in viscosity between UV-aged and the control. The limitations of the predictions could be due to uncertainties in the parameters used within the parametrization. One parameter that is highly uncertain is the fragility parameter, which has a significant effect on the predicted viscosities (*SI Appendix*, Section 2). Furthermore, we assume this fragility parameter is the same for UV-aged and control SOA, which may not be correct. An important limitation that should also be noted is that this parameterization does not consider supramolecular assembly, molecular structure, or functionality explicitly. These properties are known to be important for viscosity (90, 91) and may change with UV-aging. The limitations of the predictions could also be due to uncertainties in the assumptions used to calculate relative abundance of each compound in the SOA mixture from the high-resolution mass spectrometry data. A more detailed discussion of these uncertainties is presented in *SI Appendix*, Section 2.

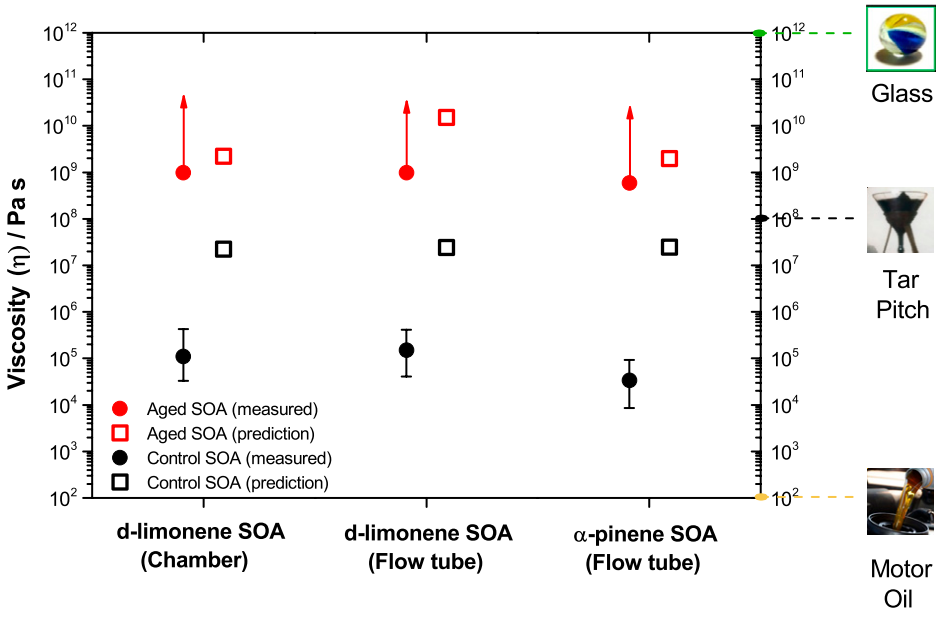

Fig. 3. Chemical composition-based viscosity predictions. Measured viscosities of ozonolysis derived control and aged SOA (red and black filled circles) along with predicted viscosities (red and black open squares) under dry conditions. Viscosities were predicted using the approach of DeRieux et al. (77) with the HRMS composition (Fig. 2 and *SI Appendix*, Figs. S6 and S7) as input. Error bars in the y-direction correspond to the upper and lower limits of viscosities from the poke-flow experiments. Upward arrows indicate lower limits.

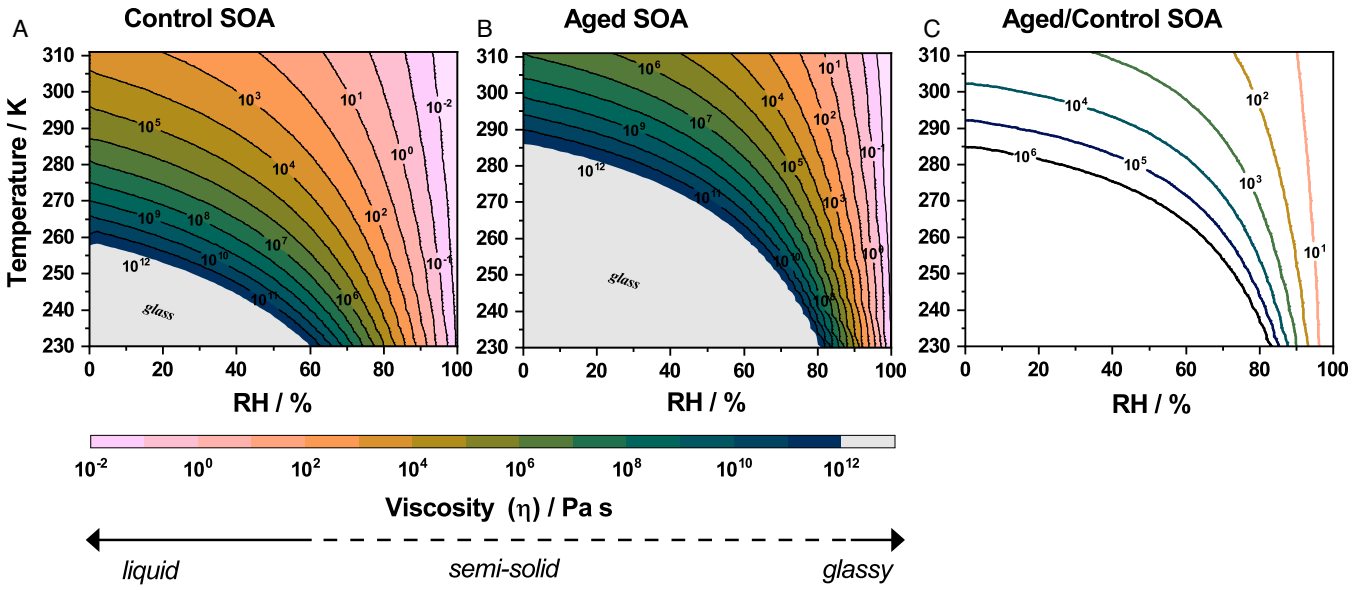

Fig. 4. Viscosity of control and aged d-limonene SOA as a function of RH and temperature. (*A* and *B*) Viscosity of control and aged d-limonene SOA, respectively, is shown. (*C*) Ratio of the viscosity of aged to control d-limonene SOA, demonstrating the increase in viscosity from UV-aging is shown. Gray-shaded areas indicate when the viscosity is larger than 10^{12} Pa s, which corresponds to a glass state. Data shown corresponds to SOA produced in an environmental chamber by ozonolysis.

A more definitive metric in comparing the effects of UV-aging on SOA viscosity is the value of T_g itself because its prediction depends on fewer parameters compared to the prediction of the sample viscosity. Predictions of T_g rely solely on the chemical formulas and relative abundances of the organics in the SOA samples. Comparing these values reveals an increase in T_g by 10.2 K, 13.7 K, and 9.8 K for environmental chamber produced d-limonene ozonolysis SOA, flow tube produced d-limonene ozonolysis SOA, and α-pinene ozonolysis SOA, respectively (*SI Appendix*, Table S3). Overall, both prediction metrics show that UV-aging of SOA results in a substantial increase in viscosity and indicate that the experimentally determined increases in viscosity can be attributed to the changes in chemical composition.

Atmospheric Implications. In the troposphere, the RH often varies from 10% to 100%, and the temperature often varies from ~205 K to 300 K (92). To extrapolate our results to other RH values and temperatures, we developed a parameterization for the viscosity of control and aged SOA as a function of both RH and temperature from our experimental room temperature data (*SI Appendix*, Section 3). Here, we focus on the results of d-limonene SOA generated in an environmental chamber (Fig. 4 *A* and *B*), but similar results are expected for d-limonene SOA and α-pinene SOA generated in a flow tube. The parameterization as a function of both RH and temperature revealed that the viscosity of SOA particles, especially after UV-aging, can be very high when the temperature is below 285 K and the RH is below 80% (Fig. 4 *A* and *B*). The parameterization also shows that UV-aging will increase viscosity by several orders of magnitude for a range of RH and temperature conditions (Fig. 4*C*).

To estimate zonally averaged SOA particle viscosities in the troposphere, we combined the parameterization for the viscosity of control and aged SOA as a function of RH and temperature (Fig. 4 *A* and *B*) with annual averaged RH and temperature profiles in the troposphere from a global climate chemistry model for the years 2005 to 2009 (63). Details are given in *SI Appendix*, Section 3. The results are shown in Fig. 5. After UV-aging, viscosities are high ($\eta > 10^6$ Pa s) for most parts of the free troposphere (1–18 km) (Fig. 5*B*). In addition, viscosities are often several orders of magnitude larger for aged SOA compared to control SOA at the same altitude (Fig. 5*C*).

The viscosities of SOA can be used to infer the phase state of the SOA particles (Fig. 5). SOA will be liquid when the viscosity is below 10^2 Pa s, semisolid when the viscosity is between 10^2 to 10^{12} Pa s, and glassy solid when the viscosity is greater than 10^{12} Pa s (89). On average, control SOA will mostly be in a liquid state below about 2 km, a semisolid state between 2 and 8 km, and a glassy solid state at altitudes above 8 km (Fig. 5*A*). In contrast, after UV-aging, the SOA particles will most often have a liquid state at 1 km and below, a semisolid state between 1 and 6 km, and a glassy solid state above 6 km (Fig. 5*B*).

While the role of organic aerosols for ice nucleation is still a matter of ongoing debate (3), one key conclusion emerging from previous studies (52, 93–101) is that the phase state of organic particles strongly affects their ice nucleation ability, with organic aerosol particles requiring highly viscous or glassy solid states to potentially act as heterogeneous nuclei for ice clouds (53, 93, 95, 100). As discussed above, UV-aging leads to a glassy solid state at ~2 km lower altitudes in the troposphere (Fig. 5). Therefore, if the effects of UV-aging on SOA viscosity observed here extend to atmospheric SOA, such aging processes could denote unrecognized sources of nuclei for ice clouds, with important implications for Earth's energy budget and climate.

Mixing times of organic molecules within SOA particles are important for predicting the growth, evaporation, and size distribution of SOA, and hence, air pollution and climate. It is often assumed in chemical transport models, which are used to assess air quality and aerosol-climate effects, that the mixing of organic molecules within SOA particles occurs faster than the time step used in the models, which is on the order of 0.5 to 1 h (52, 102). To estimate mixing times of organic molecules within SOA particles from our viscosity data, we used the zonally averaged viscosities shown in Fig. 5 to estimate mixing times of organic molecules within SOA particles with a diameter of 200 nm (Fig. 6). Details are given in *SI Appendix*, Section 3. A particle diameter of 200 nm was used to represent typical atmospheric accumulation mode SOA particles (1). Our results, shown in Fig. 6, reveal that after UV-aging, mixing times within

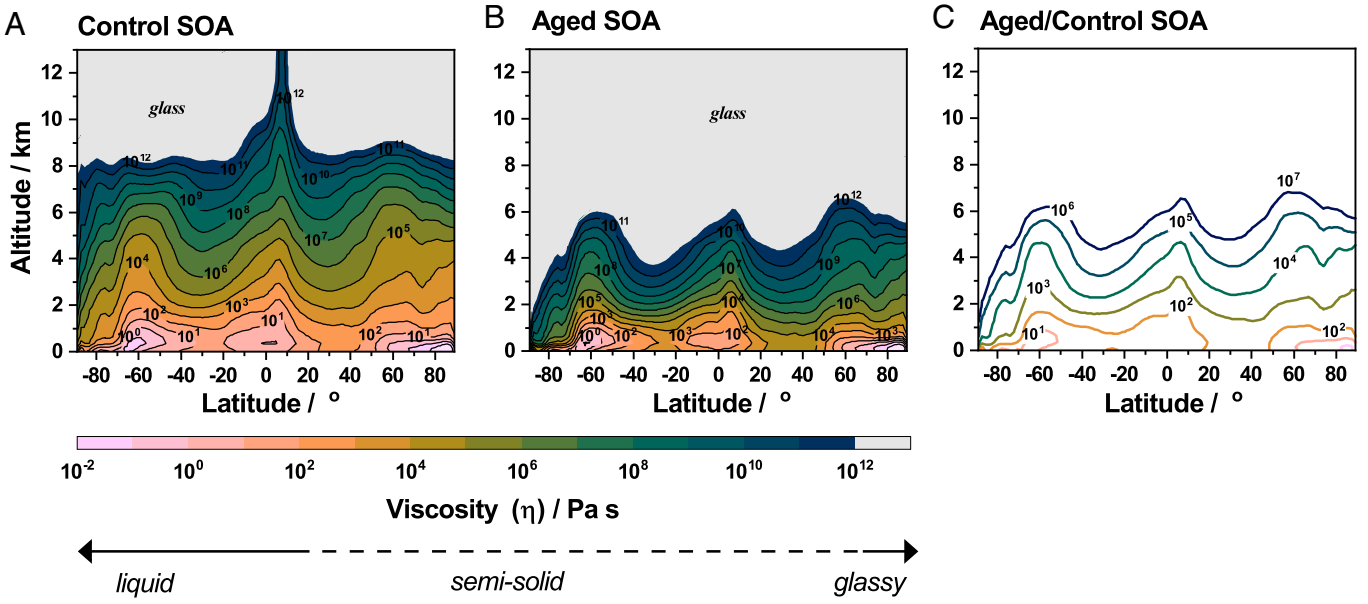

Fig. 5. Zonally averaged SOA viscosity as a function of altitude and latitude in the troposphere. A comparison of the effect of aging by UV-radiation on the zonally averaged SOA viscosity as a function of altitude and latitude in the troposphere. (*A* and *B*) Viscosity for control and aged d-limonene SOA, respectively, is shown. (*C*) Ratio of viscosity of aged and control d-limonene SOA is shown. Gray-shaded areas indicate viscosities were above 10^{12} Pa s, which corresponds to a glassy phase state. Data shown correspond to SOA produced in an environmental chamber by ozonolysis.

200 nm SOA particles can often be larger than 0.5 h for most parts of the free troposphere contrary to the assumptions frequently used in chemical transport models. Furthermore, the mixing times after UV-aging is several orders of magnitude longer than for control SOA (Fig. 6*C*). Hence, UV-aging should be considered when estimating mixing times of organic molecules within SOA and when modeling the growth, evaporation, and size distributions of SOA.

Mixing times of water molecules within SOA particles are important for predicting if the particles are in equilibrium with the surrounding water vapor. We determined zonally averaged mixing times of water molecules within SOA particles with a diameter of 200 nm. Our results (*SI Appendix*, Section S3, Fig. S9) show that the mixing times of water are several orders of magnitude longer in UV-aged SOA particles compared to the control SOA particles (*SI Appendix*, Fig. S9). In addition, mixing times of water are often very short (<0.001 h) below 4 km for the UV-aged particles. At these altitudes, the UV-aged particles are likely often in near equilibrium with the surrounding water vapor. On the other hand, at altitudes above 6 km, the mixing times of water in UV-aged particles most often exceed 0.1 h. In this case, a glassy state can persist sufficiently long in air parcel updrafts to act as a heterogeneous ice nucleus (103).

While our findings indicate that UV-aging of d-limonene and α-pinene derived SOA leads to an increase in viscosity, our modeling studies did not account for the change in mass loading

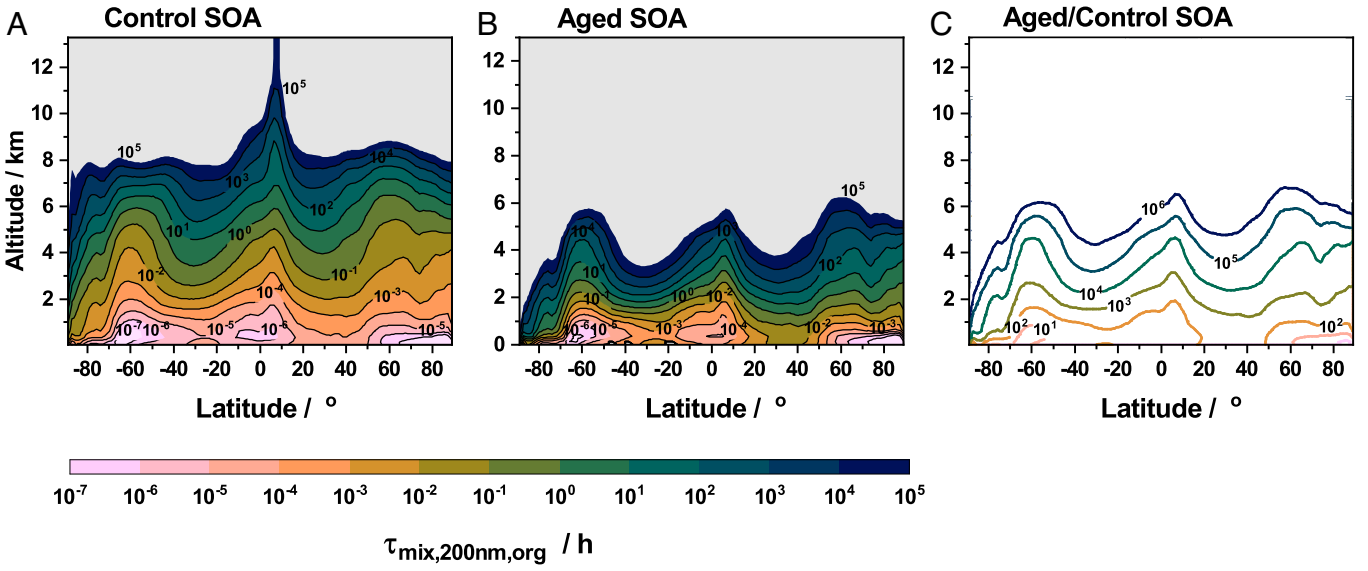

Fig. 6. Zonally averaged mixing times of organic molecules within 200 nm SOA. A comparison of the effect of aging by UV-radiation on the zonally averaged mixing times of organic molecules within 200 nm SOA. (*A* and *B*) Spatial distribution of mixing times of organic molecules for control and aged d-limonene SOA, respectively. (*C*) Ratio of mixing times of organic molecules of aged and control d-limonene SOA. Gray-shaded areas indicate that mixing times of organic molecules were not determined; since the viscosities used to calculate mixing times were above 10^{12} Pa s, and the Vogel-Tammann-Fulcher equation does not accurately predict viscosities above 10^{12} Pa s. Data shown correspond to SOA produced in an environmental chamber by ozonolysis.

with altitude and other atmospheric aging processes (62). In tandem, these processes would lead to even lower viscosities than predicted with our parameterization. Further studies are necessary with SOA generated with lower mass loadings. Additional studies are also needed to determine if our findings apply to other aerosol types, such as SOA from isoprene and aromatic hydrocarbons and aerosols from biomass burning. Also, studies are necessary to determine the effect of UV-aging on the ice nucleating ability of SOA.

In summary, this study makes the first attempt to quantify the effect and magnitude of UV-aging on the viscosity of SOA particles. Our results show that aging of SOA by exposure to UV-radiation over multiple days can increase viscosity by several orders of magnitude or more. The increased viscosity likely leads to increased abundance of SOA in a glassy solid state that can potentially act as ice nucleation particles and impact ice cloud formation and climate. In addition, our results show that the mixing times of organic molecules within a SOA particle increase significantly after UV-aging, with implications for predicting of growth, evaporation, and the size distribution of SOA. Overall, our results underscore the need to consider the effects of UV-aging when predicting the properties of SOA and their environmental impacts.

Materials and Methods

Section 1: SOA Production and Collection. SOA was prepared by dark ozonolysis in either an environmental chamber or a flow tube. The environmental chamber consisted of a 5 m^3 Teflon bag and was operated in batch mode. In the environmental chamber experiments, a solution of liquid d-limonene (Fischer Scientific, 97% purity) in methanol (Thermo Scientific, Optima LC/MS Grade) (1:10 vol/vol) was injected into a glass bulb, and a particle- and hydrocarbon-free airflow (3 L min^{-1}) from a zero-air generator (Parker, FTIR purge gas generator model 75-62NA) was used to carry the organic vapors through a heated inlet (T = 300 K) into the chamber. Ozone (O_3) was injected into the chamber using an ozone generator (Ozontech, OZ2SS-SS). The VOC and O_3 mixing ratios within the chamber were ∼200 ppb and 7 ppm, respectively, at the start of an experiment and the RH was 40%. SOA particles were collected from the chamber once maximum mass concentrations in the range of ∼290 to 600 μg m^{-3} were reached, corresponding to a residence time of 40 min. The mass concentration during the collection time was ∼250 μg m^{-3}. A scanning mobility particle sizer (SMPS, TSI Inc., model 3080 DMA and 3775 CPC) and a proton-transfer-reaction mass spectrometer (PTR-MS) were used to continuously monitor particle number and VOC concentrations within the chamber, respectively.

The aerosol flow tube consisted of a 20 L Plexiglas tube. A syringe pump (World Precision Instruments, Model: SP100I) was used to inject (25 μL h^{-1}) liquid α-pinene (Sigma-Aldrich, 98% purity) or d-limonene (Fischer Scientific, 97% purity) into a Swagelok T-fitting that was flushed (5 L min^{-1}) with air from a zero-air generator (Parker, FTIR purge gas generator model 75-62NA). A 1 L min^{-1} flow of oxygen was passed through an ozone generator and homebuilt ozone photometric detector before mixing with the VOC airflow within the flow tube. The starting mixing ratios of VOC and O_3 were ∼11 ppm and 7 ppm, respectively. At the start of an experiment, the RH was 0%. The residence time within the flow tube was 3.5 min, and the SOA mass concentration was ∼1.7 mg m^{-3}.

At the exit of the chamber and the flow tube, the SOA containing airflow was passed through a charcoal denuder to denude excess O_3. SOA particles were then collected either onto poly(tetrafluoroethylene; PTFE) filters (FGLP04700, Millipore, 47 mm diameter, 0.2 mm pore diameter) for HRMS analysis, or onto hydrophobic glass slides (12 mm diameter, Hampton Research, HR3-277) for viscosity and phase behavior experiments. SOA particles were collected on the hydrophobic slides using stage 8 of a nonrotating microorifice uniform deposit impactor (MOUDI; MSP Corp. model 110-R) operated at a flow rate of 20 L min^{-1}. With the remaining stages removed the resulting 50% cutoff diameter was below 180 nm. Sampling with the nonrotating MOUDI created discrete spots of aggregated SOA particles of ∼35 to 60 μm in diameter after a typical collection time of 1 h.

Glass slides were made hydrophobic by coating with FluoroPel-800 (Cytonix). A control experiment was conducted to ensure that 12 d of UV exposure (the same exposure used for the SOA samples) did not degrade the hydrophobic coating and inadvertently effect the viscosity measurements. See *SI Appendix*, Fig. S10 for details.

Section 2: UV-Aging of SOA Particles. Aging was achieved by placing the SOA-containing substrates (filters or hydrophobic glass slides) into an irradiation chamber (*SI Appendix*, Fig. S11). The irradiation chamber was continuously flushed (860 cm^3 min^{-1}) with air from a zero-air generator (Parker, FTIR purge gas generator model 75-62NA), to remove any volatile products formed during photoaging. The irradiation chamber was separated into two compartments using a high-purity aluminum foil barrier (Sigma Aldrich, 99.999% purity, 1.0 mm thickness). One compartment was equipped with a UV-LED, and the other compartment was kept dark to simultaneously produce an aged and a control SOA sample, respectively. This separation ensured that the control (unaged) sample experienced the same amount of evaporative loss as the aged (irradiated) sample. This approach allowed us to cleanly separate the effects of UV exposure from evaporative aging. It is important to note that in the atmosphere, SOA particles will also be exposed to gas-phase oxidants (e.g., ozone and OH radicals), which can further impact the particle viscosity.

The incident power of the LED (Thorlabs Inc., model M300L4) was 2.4 mW, measured using a power meter (Coherent PS19Q) at the same distance between the LED and the SOA containing substrate (3.4 cm vertical distance between LED and substrate). With the 2.8 cm^2 area of the power meter, this corresponds to a peak spectral flux of 1.0×10^{15} photons cm^{-2} s^{-1}. Previous experiments demonstrated that similar power meter measurements agree with actinometry experiments (24, 30). This compares reasonably well to the flux of 4.1×10^{14} photons cm^{-2} s^{-1} additionally measured with a radiometer (StellarNet Inc., Black-Comet UV-VIS Spectrometer). To age an SOA sample, it was irradiated with the LED centered at $\lambda = 305$ nm for 12 d. This equals to an exposure of ∼6 to 14 d in Los Angeles, CA, based on the overlap of the UV-LED spectral flux density with the 24 h average (including day and night) spectral flux density in Los Angeles from 290 to 330 nm (on June 20, 2017; *SI Appendix*, Fig. S12). An irradiation time of 12 d was chosen to ensure the formation of a nondegrading, photo-recalcitrant fraction, as determined by Baboomian et al. (28). Here, a 305 nm LED was used instead of a full solar spectrum, in order to target the $n \rightarrow \pi^*$ carbonyl transitions in photolabile compounds, which lead to Norrish type I and II reactions (30, 79). In addition, using an LED instead of a solar simulator avoids heating of the sample with visible and near-infrared radiation. The irradiation chamber reached temperatures of ∼22 °C when the LED was on. Thus, we do not expect any considerable temperature effects on the SOA viscosity within the experiment. Equally important, by using a 305 nm LED and in the absence of nitrogen oxides (NO_x), gas-phase ozone is not produced in the irradiation chamber. This ensures that free radical formation through photodegradation of the SOA molecules is the main driver of the aging process.

Section 3: Measurement of SOA Viscosity as a Function of Relative Humidity. After aging was completed, SOA samples were shipped overnight over ice packs from the University of California, Irvine to the University of British Columbia for viscosity measurements. We do not expect sample transportation to have affected the measured viscosity values as the samples were sent, received, and stored in a freezer within 24 h, which is a short time relative to UV exposure times. If further aging were to occur within the shipping times, these changes to SOA composition would be humidity-, temperature-, or radiation-driven. Wong et al. (104) showed that on a time scale of 2 d, even in the presence of humidity and room temperature, SOA chemical changes were not too significant. Furthermore, any possible radiation-driven changes that may have occurred during transport would further emphasize our results on the importance of radiation driven changes in viscosity.

The viscosity of the particles was measured at different RH values using the poke-flow technique (52, 54, 57, 105). For the poke-flow experiments, a slide with SOA particles was placed into a RH-controlled flow cell coupled to an inverted optical microscope (AmScope, model ME1400TC-INF). The SOA particles were conditioned at the respective RH of the poke-flow experiment by continuously passing a flow (∼0.5 L min^{-1}) of dry or humidified nitrogen (Praxair, 5.0 grade) over the particles. The dew point within the flow cell was continuously monitored using a

hygrometer (Hygro M4/E4, General Eastern Instruments). Similarly, the temperature of the flow cell was continuously monitored using a thermocouple (Omega, model: FF-T-20-100) and maintained at T = 292 ± 0.3 K for all experiments. The RH within the flow cell was calculated from the measured dewpoint and temperature. For most experiments, the SOA particles were conditioned at the respective RH for 2 h. In addition, for SOA generated by ozonolysis of d-limonene in an environmental chamber, conditioning times ranging from 1 to 24 h were used (*SI Appendix*, Fig. S3). Viscosities were identical within the uncertainties after conditioning for 1 to 24 h, indicating that a conditioning time of 2 h is sufficient for near equilibrium conditions. Also, separate tests showed that evaporation of the SOA particles during the poke-flow experiments, even after 24 h, was less than could be detected with our optical microscope (*SI Appendix*, Fig. S2).

During poke flow measurements, SOA particles with diameters of ∼35 to 60 μm were poked with a tungsten needle (20 μm diameter, Roboz Surgical Instruments Co.) coated to make it oleophobic (Cytonix, OilSlip 110). The morphology of the poked particles was continuously monitored using a CCD camera, capturing images at a rate of three frames per second. Poking introduced a hole within the particles, usually leading to particles with a half-torus geometry. After poking, the particle material flowed and returned to its energetically preferred spherical cap geometry. The time required for the area of the hole (A) to decrease to one quarter of its initial size, referred to as the experimental flow time ($\tau_{exp,flow}$), was determined and used to extract the particle viscosity (52, 106). For highly viscous ($\eta \gtrsim 10^8$ Pa s) particles that did not flow, a lower limit of $\tau_{exp,flow}$ was obtained, by assuming the radius of the initial hole decreased by 0.5 μm during the observation time in the experiments. Lower limit experimental flow times are denoted by upward pointing arrows (e.g., *SI Appendix*, Fig. S1). A decrease of 0.5 μm in radius defines the spatial resolution of the microscope and corresponds to a change in area of ∼5% to 10%. For particles that cracked upon poking, a lower limit of $\tau_{exp,flow}$ was obtained by assuming one of the edges of the cracked particle moved by 0.5 μm during the observation time in the experiments. These cases also denote lower limits and are thus also denoted by upwards pointing arrows (*SI Appendix*, Fig. S1). Conversely, for particles with very low viscosities ($\eta < 10^3$ Pa s), $\tau_{exp,flow}$ was shorter than the time between images captured with the CCD camera. In these cases, an upper limit of $\tau_{exp,flow}$ was obtained by setting $\tau_{exp,flow}$ as the time between images. Upper limit flow times are denoted by downward pointing arrows (*SI Appendix*, Fig. S1).

To obtain viscosities from the experimental flow times, fluid dynamics modeling was performed to simulate the flow of the material in the poke flow experiments, using the COMSOL Multiphysics software (COMSOL Inc., v5.4), as detailed previously (106). Within the model, the flow of the SOA material was simulated using the observed $\tau_{exp,flow}$ as an input parameter, together with the following material properties: density, slip length, surface tension, and contact angle (54). The values of these material properties are summarized in *SI Appendix*, Table S2. The particle viscosity in the COMSOL simulations were varied until the modeled flow time ($\tau_{mod,flow}$) agreed with the experimental flow time ($\tau_{exp,flow}$) to within 1%. Changes in the slip length had the largest effect on the derived viscosity, followed by surface tension, and lastly contact angle. In our COMSOL simulations the slip length, surface tension, and contact angle parameters were systematically varied in order to obtain upper and lower bounds for the SOA viscosity. In our COMSOL simulations, we assumed the SOA particles were homogeneous (i.e., consisted of a single phase) for all the RHs used for the viscosity measurements. This assumption was confirmed using optical microscopy (although we have to acknowledge that optical microscopy is unlikely to capture inhomogeneities due to viscosity gradients, if present). Details are given in *SI Appendix*, Section 5.

Section 4: HRMS Analysis. The HRMS data were obtained using ultra-performance liquid chromatography (UPLC) coupled with a Thermo Q Exactive Plus orbitrap mass spectrometer equipped with an electrospray ionization (ESI) source. The UPLC-ESI-HRMS was operated in negative ion mode with a mass resolving power of $\sim 10^5$ at *m/z* 200, and a spray voltage of 2.5 kV. Only negative ion mode data were analyzed since the mass spectrometer was more sensitive in the negative ion mode and positive ion mode did not provide much additional information. The extraction solvent consisted of a 1:1 (vol/vol) mixture of acetonitrile (Sigma Aldrich, purity ≥ 99.9%) and water (Sigma-Aldrich, HPLC grade). SOA were extracted from the PTFE-filters, by submerging each filter in 15 mL of solvent within an orbital shaker (Thermolyne, 37600 Mixer) for 15 min, followed by dilution, achieving typical concentrations of around 400 μg mL^{-1}. A Luna 1.6 μm Omega Polar C_{18} (150 × 2.1 mm) column was used for separation. Solvents A and B used during liquid chromatography were HPLC grade acetonitrile (with 0.1% formic acid) and water (0.1% formic acid), respectively. The gradient elution protocol included a 3 min hold at 5% solvent A, an 11 min linear gradient to 95% solvent A, a 2 min hold at this level, and a linear gradient back to 5% solvent A in preparation for the next run. The column was maintained at 30 °C.

Sections of the ion chromatogram with strong analyte intensity (intensity < 1×10^7) were integrated (3 to 16 min). Each PTFE filter extraction was run in triplicate through the instrument and only HRMS-peaks that appeared in all three trials were used for molecular assignment. In addition to the samples, a solvent blank was prepared following the same procedure above but using a control substrate without analyte.

The method applied here combining/coupling UPLC and HRMS is more accurate in measuring relative ion abundances due to the chromatographic separation, compared to our previous study, where we utilized direct infusion of the analyte containing solvent into the MS-inlet, which is prone to matrix effects (28). Matrix effects due to direct infusion have been shown to result in changes in the ionization efficiency of analytes, ion suppression through charge competition, or enhancement due to the presence of certain compounds, such as inorganic salts (86–88). Thus, separating compounds before the ionization source can be effective in reducing the artifacts of direct infusion (86).

HRMS-peaks were assigned molecular formulas following previous work (23, 28). HRMS-peak positions and relative abundances were extracted using the Decon2LS software package and peaks containing ^{13}C isotopes were removed. All HRMS-peaks were assigned to the formulas $C_xH_yO_z$ with an accuracy of ±0.001 *m/z* units while constraining the assignments to H/C of 0.30 to 2.25 and O/C of 0.00 to 2.30. Assignments were also constrained to closed-shell ions with even nominal masses. The assigned ion formulas were corrected for the ionization mechanism. The assumed ionization mechanism was deprotonation of the molecular compounds resulting in $[M\text{-}H]^-$ for negative ions. All the HRMS results are reported as formulas of neutral SOA compounds.

Data, Materials, and Software Availability. All study data are included in the article and/or supporting information.

ACKNOWLEDGMENTS. This work was supported by US NSF through grants AGS-1853639 (V.J.B., S.A.N.) and AGS-1654104 (M.S.), and by Natural Sciences and Engineering Research Council of Canada (NSERC) through grant RGPIN/04441-2016 (G.V.C., A.K.B., Y.H.). F.M. received funding from the European Union's Horizon 2020 research and innovation programme under the Marie Skłodowska-Curie grant agreement No. 890200. The high-resolution mass spectrometer instrument used in this work was purchased with grant NSF CHE-1920242. V.J.B. thanks the NSF GRFP program for his graduate fellowship. We thank Natalie R. Smith for help with preparation of the sample collection substrates. The Scientific colour map Batlow was used in this study to prevent visual distortion of the data and exclusion of readers with color-vision deficiencies.

1. B. J. Finlayson-Pitts, J. N. Pitts, *Chemistry of the Upper and Lower Atmosphere: Theory, Experiments, and Applications* (Academic Press, 2000).
2. IPCC, Climate Change 2013: The Physical Science Basis. Contribution of Working Group I to the Fifth Assessment Report of the Intergovernmental Panel on Climate Change. Stocker, T.F., D. Qin, G.-K. Plattner, M. Tignor, S.K. Allen, J. Boschung, A. Nauels, Y. Xia, V. Bex and P.M. Midgley, Eds. (Cambridge University Press, Cambridge), pp. 1535.
3. D. A. Knopf, P. A. Alpert, B. Wang, The role of organic aerosol in atmospheric ice nucleation: A review. *ACS Earth Space Chem.* 10.1021/acsearthspacechem.7b00120. (2018).
4. M. Kanakidou *et al.*, Organic aerosol and global climate modelling: A review. *Atmos. Chem. Phys.* **5**, 1053–1123 (2005).
5. C. A. Pope, 3rd, M. Ezzati, D. W. Dockery, Fine-particulate air pollution and life expectancy in the United States. *N. Engl. J. Med.* **360**, 376–386 (2009).
6. C. A. Pope, 3rd, D. W. Dockery, Health effects of fine particulate air pollution: Lines that connect. *J. Air Waste Manag. Assoc.* **56**, 709–742 (2006).
7. A. J. Haagen-Smit, Chemistry and physiology of Los Angeles smog. *Ind. Eng. Chem.* **44**, 1342–1346 (1952).
8. J. Lelieveld, J. S. Evans, M. Fnais, D. Giannadaki, A. Pozzer, The contribution of outdoor air pollution sources to premature mortality on a global scale. *Nature* **525**, 367–371 (2015).
9. J. Lelieveld *et al.*, Loss of life expectancy from air pollution compared to other risk factors: A worldwide perspective. *Cardiovasc. Res.* **116**, 1910–1917 (2020).

10. D. v. Spracklen *et al.*, Aerosol mass spectrometer constraint on the global secondary organic aerosol budget. *Atmos. Chem. Phys.* **11**, 12109–12136 (2011).
11. M. Hallquist *et al.*, The formation, properties and impact of secondary organic aerosol: Current and emerging issues. *Atmos. Chem. Phys.* **9**, 5155–5236 (2009).
12. A. B. Guenther *et al.*, The model of emissions of gases and aerosols from nature version 2.1 (MEGAN2.1): An extended and updated framework for modeling biogenic emissions. *Geosci. Model Dev.* **5**, 1471–1492 (2012).
13. Y. J. Balkanski, D. J. Jacob, G. M. Gardner, W. C. Graustein, K. K. Turekian, Transport and residence times of tropospheric aerosols inferred from a global three-dimensional simulation of 210Pb. *J. Geophys. Res.* **98**, 20573–20586 (1993).
14. R. Jaenicke, Atmospheric aerosols and global climate. *J. Aerosol Sci.* **11**, 577–588 (1980).
15. S. Brönnimann, *Climate of the Free Troposphere and Mountain Peaks. Oxford Research Encyclopedia of Climate Science* (Oxford University Press, 2020).
16. K. Tsigaridis, M. Kanakidou, Global modelling of secondary organic aerosol in the troposphere: A sensitivity analysis. *Atmos. Chem. Phys.* **3**, 1849–1869 (2003).
17. I. J. George, J. P. D. Abbatt, Heterogeneous oxidation of atmospheric aerosol particles by gas-phase radicals. *Nat. Chem.* **2**, 713–722 (2010).
18. S. H. Kessler *et al.*, OH-initiated heterogeneous aging of highly oxidized organic aerosol. *J. Phys. Chem. A* **116**, 6358–6365 (2012).
19. I. J. George, J. P. D. Abbatt, Chemical evolution of secondary organic aerosol from OH-initiated heterogeneous oxidation. *Atmos. Chem. Phys.* **10**, 5551–5563 (2010).
20. D. Aljawhary, R. Zhao, A. K. Y. Lee, C. Wang, J. P. D. Abbatt, Kinetics, mechanism, and secondary organic aerosol yield of aqueous phase photo-oxidation of α-pinene oxidation products. *J. Phys. Chem. A* **120**, 1395–1407 (2016).
21. R. F. Hems, J. P. D. Abbatt, Aqueous phase photo-oxidation of brown carbon nitrophenols: Reaction kinetics, mechanism, and evolution of light absorption. *ACS Earth Space Chem.* **2**, 225–234 (2018).
22. D. E. Romonosky *et al.*, Aqueous photochemistry of secondary organic aerosol of α-pinene and α-humulene oxidized with ozone, hydroxyl radical, and nitrate radical. *J. Phys. Chem. A* **121**, 1298–1309 (2017).
23. A. L. Klodt *et al.*, Aqueous photochemistry of secondary organic aerosol of α-pinene and α-humulene in the presence of hydrogen peroxide or inorganic salts. *ACS Earth Space Chem.* **3**, 2736–2746 (2019).
24. K. T. Malecha, S. A. Nizkorodov, Feasibility of photosensitized reactions with secondary organic aerosol particles in the presence of volatile organic compounds. *J. Phys. Chem. A* **121**, 4961–4967 (2017).
25. M. E. Monge *et al.*, Alternative pathway for atmospheric particles growth. *Proc. Natl. Acad. Sci. U.S.A.* **109**, 6840–6844 (2012).
26. X. Wang *et al.*, Atmospheric photosensitization: A new pathway for sulfate formation. *Environ. Sci. Technol.* **54**, 3114–3120 (2020).
27. X. Wang *et al.*, Naphthalene-derived secondary organic aerosols interfacial photosensitizing properties. *Geophys. Res. Lett.* e2021GL093465 (2021) 10.1029/2021gl093465.
28. V. J. Baboomian, Y. Gu, S. A. Nizkorodov, Photodegradation of secondary organic aerosols by long-term exposure to solar actinic radiation. *ACS Earth Space Chem.* **4**, 1078–1089 (2020).
29. E. Q. Walhout, H. Yu, C. Thrasher, J. M. Shusterman, R. E. O'Brien, Effects of photolysis on the chemical and optical properties of secondary organic material over extended time scales. *ACS Earth Space Chem.* **3**, 1226–1236 (2019).
30. K. T. Malecha, S. A. Nizkorodov, Photodegradation of secondary organic aerosol particles as a source of small, oxygenated volatile organic compounds. *Environ. Sci. Technol.* **50**, 9990–9997 (2016).
31. K. T. Malecha, Z. Cai, S. A. Nizkorodov, Photodegradation of secondary organic aerosol material quantified with a quartz crystal microbalance. *Environ. Sci. Technol. Lett.* **5**, 366–371 (2018).
32. P. C. Arroyo, K. T. Malecha, M. Ammann, S. A. Nizkorodov, Influence of humidity and iron(iii) on photodegradation of atmospheric secondary organic aerosol particles. *Phys. Chem. Chem. Phys.* **20**, 30021–30031 (2018).
33. H. Lignell *et al.*, Experimental and theoretical study of aqueous cis-pinonic acid photolysis. *J. Phys. Chem. A* **117**, 12930–12945 (2013).
34. S. A. Epstein, S. L. Blair, S. A. Nizkorodov, Direct photolysis of α-pinene ozonolysis secondary organic aerosol: Effect on particle mass and peroxide content. *Environ. Sci. Technol.* **48**, 11251–11258 (2014).
35. R. F. Hems, E. G. Schnitzler, C. Liu-Kang, C. D. Cappa, J. P. D. Abbatt, Aging of atmospheric brown carbon aerosol. *ACS Earth Space Chem.* **5**, 722–748 (2021).
36. V. Pospisilova *et al.*, Photodegradation of α-pinene secondary organic aerosol dominated by moderately oxidized molecules. *Environ. Sci. Technol.* **55**, 6936–6943 (2021).
37. M. A. Zawadowicz *et al.*, Photolysis controls atmospheric budgets of biogenic secondary organic aerosol. *Environ. Sci. Technol.* **54**, 3861–3870 (2020).
38. J. P. Reid *et al.*, The viscosity of atmospherically relevant organic particles. *Nat. Commun.* **9**, 1–14 Article number: 956 (2018).
39. M. Shiraiwa, M. Ammann, T. Koop, U. Pöschl, Gas uptake and chemical aging of semisolid organic aerosol particles. *Proc. Natl. Acad. Sci. U.S.A.* **108**, 11003–11008 (2011).
40. Y. Li, M. Shiraiwa, Timescales of secondary organic aerosols to reach equilibrium at various temperatures and relative humidities. *Atmos. Chem. Phys.* **19**, 5959–5971 (2019).
41. P. Liu *et al.*, Highly viscous states affect the browning of atmospheric organic particulate matter. *ACS Cent. Sci.* **4**, 207–215 (2018).
42. Y. J. Li *et al.*, Chemical reactivity and liquid/nonliquid states of secondary organic material. *Environ. Sci. Technol.* **49**, 13264–13274 (2015).
43. A. Zelenyuk *et al.*, Synergy between secondary organic aerosols and long-range transport of polycyclic aromatic hydrocarbons. *Environ. Sci. Technol.* **46**, 12459–12466 (2012).
44. Q. Mu *et al.*, Temperature effect on phase state and reactivity controls atmospheric multiphase chemistry and transport of PAHs. *Sci. Adv.* **4**, eaap7314 (2018).
45. I. J. Keyte, R. M. Harrison, G. Lammel, Chemical reactivity and long-range transport potential of polycyclic aromatic hydrocarbons – A review. *Chem. Soc. Rev.* **42**, 9333–9391 (2013).
46. M. Shrivastava *et al.*, Global long-range transport and lung cancer risk from polycyclic aromatic hydrocarbons shielded by coatings of organic aerosol. *Proc. Natl. Acad. Sci. U.S.A.* **114**, 1246–1251 (2017).
47. C. L. Friedman, J. R. Pierce, N. E. Selin, Assessing the influence of secondary organic versus primary carbonaceous aerosols on long-range atmospheric polycyclic aromatic hydrocarbon transport. *Environ. Sci. Technol.* **48**, 3293–3302 (2014).
48. P. A. Alpert *et al.*, Photolytic radical persistence due to anoxia in viscous aerosol particles. *Nat. Commun.* **12**, 1769 (2021).
49. H. Lignell, M. L. Hinks, S. A. Nizkorodov, Exploring matrix effects on photochemistry of organic aerosols. *Proc. Natl. Acad. Sci. U.S.A.* **111**, 13780–13785 (2014).
50. R. A. Zaveri *et al.*, Rapid growth of anthropogenic organic nanoparticles greatly alters cloud life cycle in the Amazon rainforest. *Sci. Adv.* **8**, eabj0329 (2022).
51. M. J. Wolf *et al.*, A biogenic secondary organic aerosol source of cirrus ice nucleating particles. *Nat. Commun.* **11**, 4834 (2020).
52. L. Renbaum-Wolff *et al.*, Viscosity of α-pinene secondary organic material and implications for particle growth and reactivity. *Proc. Natl. Acad. Sci. U.S.A.* **110**, 8014–8019 (2013).
53. B. J. Murray *et al.*, Heterogeneous nucleation of ice particles on glassy aerosols under cirrus conditions. *Nat. Geosci.* **3**, 233–237 (2010).
54. J. W. Grayson *et al.*, Effect of varying experimental conditions on the viscosity of α-pinene derived secondary organic material. *Atmos. Chem. Phys.* **16**, 6027–6040 (2016).
55. A. Pajunoja *et al.*, Estimating the viscosity range of SOA particles based on their coalescence time. *Aerosol Sci. Technol.* **48**, i–iv (2014).
56. W. M. Champion, N. E. Rothfuss, M. D. Petters, A. P. Grieshop, Volatility and viscosity are correlated in terpene secondary organic aerosol formed in a flow reactor. *Environ. Sci. Technol. Lett.* **6**, 513–519 (2019).
57. A. M. Maclean *et al.*, Humidity-dependent viscosity of secondary organic aerosol from ozonolysis of β-caryophyllene: Measurements, predictions, and implications. *ACS Earth Space Chem.* **5**, 305–318 (2021).
58. M. Song *et al.*, Liquid-liquid phase separation and viscosity within secondary organic aerosol generated from diesel fuel vapors. *Atmos. Chem. Phys.* **19**, 12515–12529 (2019).
59. Y. Li, A. G. Carlton, M. Shiraiwa, Diurnal and seasonal variations in the phase state of secondary organic aerosol material over the contiguous US simulated in CMAQ. *ACS Earth Space Chem.* **5**, 1971–1982 (2021).
60. A. M. Maclean *et al.*, Mixing times of organic molecules within secondary organic aerosol particles: A global planetary boundary layer perspective. *Atmos. Chem. Phys.* **17**, 13037–13048 (2017).
61. R. Schmedding *et al.*, Predicting secondary organic aerosol phase state and viscosity and its effect on multiphase chemistry in a regional-scale air quality model. *Atmos. Chem. Phys.* **20**, 8201–8225 (2020).
62. M. Shiraiwa *et al.*, Global distribution of particle phase state in atmospheric secondary organic aerosols. *Nat. Commun.* **8**, 15002 (2017).
63. A. M. Maclean *et al.*, Global distribution of the phase state and mixing times within secondary organic aerosol particles in the troposphere based on room-temperature viscosity measurements. *ACS Earth Space Chem.* **5**, 3458–3473 (2021).
64. S. Madronich, Tropospheric ultraviolet and visible (TUV) radiation model. https://www2.acom.ucar.edu/modeling/tropospheric-ultraviolet-and-visible-tuv-radiation-model. Accessed 17 November 2021.
65. S. Madronich, S. Flocke, "The role of solar radiation in atmospheric chemistry" in *Handbook of Environmental Chemistry*, P. Boule, Ed. (Springer, 1998), pp. 1–26.
66. A. Maria Yanez-Serrano *et al.*, Monoterpene chemical speciation in a tropical rainforest:variation with season, height, and time of dayat the Amazon Tall Tower Observatory (ATTO). *Atmos. Chem. Phys.* **18**, 3403–3418 (2018).
67. A. Guenther, A global model of natural volatile organic compound emissions. *J. Geophys. Res.* **100**, 8873–8892 (1995).
68. M. Capouet *et al.*, Modeling aerosol formation in alpha-pinene photo-oxidation experiments. *J. Geophys. Res. D Atmospheres* **113**, 5674–5688 (2008).
69. S. S. Petters, S. M. Kreidenweis, A. P. Grieshop, P. J. Ziemann, M. D. Petters, Temperature- and humidity-dependent phase states of secondary organic aerosols. *Geophys. Res. Lett.* **46**, 1005–1013 (2019).
70. D. A. Ullmann *et al.*, Viscosities, diffusion coefficients, and mixing times of intrinsic fluorescent organic molecules in brown limonene secondary organic aerosol and tests of the Stokes-Einstein equation. *Atmos. Chem. Phys.* **19**, 1491–1503 (2019).
71. M. L. Hinks *et al.*, Effect of viscosity on photodegradation rates in complex secondary organic aerosol materials. *Phys. Chem. Chem. Phys.* **18**, 8785–8793 (2016).
72. Y. Zhang *et al.*, Changing shapes and implied viscosities of suspended submicron particles. *Atmos. Chem. Phys.* **15**, 7819–7829 (2015).
73. T. Galeazzo *et al.*, Estimation of secondary organic aerosol viscosity from explicit modeling of gas-phase oxidation of isoprene and α-pinene. *Atmos. Chem. Phys.* **21**, 10199–10213 (2021).
74. J. P. S. Wong, S. Zhou, J. P. D. Abbatt, Changes in secondary organic aerosol composition and mass due to photolysis: Relative humidity dependence. *J. Phys. Chem. A* **119**, 4309–4316 (2015).
75. E. Bae *et al.*, Study of double bond equivalents and the numbers of carbon and oxygen atom distribution of dissolved organic matter with negative-mode FT-ICR MS. *Anal. Chem.* **83**, 4193–4199 (2011).
76. M. Gonsior *et al.*, Photochemically induced changes in dissolved organic matter identified by ultrahigh resolution fourier transform ion cyclotron resonance mass spectrometry. *Environ. Sci. Technol.* **43**, 698–703 (2009).
77. W. S. W. DeRieux *et al.*, Predicting the glass transition temperature and viscosity of secondary organic material using molecular composition. *Atmos. Chem. Phys.* **18**, 6331–6351 (2018).
78. Y. Li, D. A. Day, H. Stark, J. L. Jimenez, M. Shiraiwa, Predictions of the glass transition temperature and viscosity of organic aerosols from volatility distributions. *Atmos. Chem. Phys.* **20**, 8103–8122 (2020).
79. S. A. Mang *et al.*, Contribution of carbonyl photochemistry to aging of atmospheric secondary organic aerosol. *J. Phys. Chem. A* **112**, 8337–8344 (2008).
80. J. G. Calvert, J. N. Pitts, Jr., Photochemistry, John Wiley & Sons; 1st edition (January 1, 1966), 899.
81. R. E. O'Brien, J. H. Kroll, Photolytic aging of secondary organic aerosol: Evidence for a substantial photo-recalcitrant fraction. *J. Phys. Chem. Lett.* **10**, 4003–4009 (2019).
82. A. Vlasenko, I. J. George, J. P. D. Abbatt, Formation of volatile organic compounds in the heterogeneous oxidation of condensed-phase organic films by gas-phase OH. *J. Phys. Chem. A* **112**, 1552–1560 (2008).
83. J. D. Cope, K. A. Abellar, K. H. Bates, X. Fu, T. B. Nguyen, Aqueous photochemistry of 2-methyltetrol and erythritol as sources of formic acid and acetic acid in the atmosphere. *ACS Earth Space Chem.* **5**, 1265–1277 (2021).

84. T. B. Nguyen, A. Laskin, J. Laskin, S. A. Nizkorodov, Direct aqueous photochemistry of isoprene high-NO(x) secondary organic aerosol. *Phys. Chem. Chem. Phys.* **14**, 9702–9714 (2012).
85. D. E. Romonosky, A. Laskin, J. Laskin, S. A. Nizkorodov, High-resolution mass spectrometry and molecular characterization of aqueous photochemistry products of common types of secondary organic aerosols. *J. Phys. Chem. A* **119**, 2594–2606 (2015).
86. I. Kourtchev *et al.*, Comparison of heated electrospray ionization and nanoelectrospray ionization sources coupled to ultra-high-resolution mass spectrometry for analysis of highly complex atmospheric aerosol samples. *Anal. Chem.* **92**, 8396–8403 (2020).
87. E. Chekmeneva *et al.*, Optimization and application of direct infusion nanoelectrospray HRMS method for large-scale urinary metabolic phenotyping in molecular epidemiology. *J. Proteome Res.* **16**, 1646–1658 (2017).
88. F. M. A. Silva *et al.*, Chemotaxonomy of the Amazonian unonopsis species based on leaf alkaloid fingerprint direct infusion ESI-MS and chemometric analysis. *Article J. Braz. Chem. Soc* **27**, 599–604 (2016).
89. T. Koop, J. Bookhold, M. Shiraiwa, U. Pöschl, Glass transition and phase state of organic compounds: Dependency on molecular properties and implications for secondary organic aerosols in the atmosphere. *Phys. Chem. Chem. Phys.* **13**, 19238–19255 (2011).
90. D. S. Richards *et al.*, Ion-molecule interactions enable unexpected phase transitions in organic-inorganic aerosol. *Sci. Adv.* **6**, 5643–5661 (2020).
91. N. E. Rothfuss, M. D. Petters, Influence of functional groups on the viscosity of organic aerosol. *Environ. Sci. Technol.* **51**, 271–279 (2017).
92. A. Ruzmaikin, H. H. Aumann, E. M. Manning, Relative humidity in the troposphere with AIRS. *J. Atmos. Sci.* **71**, 2516–2533 (2014).
93. K. Ignatius *et al.*, Heterogeneous ice nucleation of viscous secondary organic aerosol produced from ozonolysis of α-pinene. *Atmos. Chem. Phys.* **16**, 6495–6509 (2016).
94. R. Wagner *et al.*, Ice cloud processing of ultra-viscous/glassy aerosol particles leads to enhanced ice nucleation ability. *Atmos. Chem. Phys.* **12**, 8589–8610 (2012).
95. T. W. Wilson *et al.*, Glassy aerosols with a range of compositions nucleate ice heterogeneously at cirrus temperatures. *Atmos. Chem. Phys.* **12**, 8611–8632 (2012).
96. B. Zobrist *et al.*, Oxalic acid as a heterogeneous ice nucleus in the upper troposphere and its indirect aerosol effect. *Atmos. Chem. Phys.* **6**, 3115–3129 (2006).
97. K. J. Baustian *et al.*, State transformations and ice nucleation in amorphous (semi-)solid organic aerosol. *Atmos. Chem. Phys.* **13**, 5615–5628 (2013).
98. J. C. Charnawskas *et al.*, Condensed-phase biogenic-anthropogenic interactions with implications for cold cloud formation. *Faraday Discuss.* **200**, 165–194 (2017).
99. L. A. Ladino, S. Zhou, J. D. Yakobi-Hancock, D. Aljawhary, J. P. D. Abbatt, Factors controlling the ice nucleating abilities of α-pinene SOA particles. *J. Geophys. Res. D Atmospheres* **119**, 9041–9051 (2014).
100. B. Wang *et al.*, The deposition ice nucleation and immersion freezing potential of amorphous secondary organic aerosol: Pathways for ice and mixed-phase cloud formation. *J. Geophys. Res. D Atmospheres* **117**, 16209 (2012).
101. G. P. Schill, D. O. De Haan, M. A. Tolbert, Heterogeneous ice nucleation on simulated secondary organic aerosol. *Environ. Sci. Technol.* **48**, 1675–1682 (2014).
102. M. Shiraiwa, J. H. Seinfeld, Equilibration timescale of atmospheric secondary organic aerosol partitioning. *Geophys. Res. Lett.* 10.1029/2012GL054008 (2012).
103. T. Berkemeier, M. Shiraiwa, U. Pöschl, T. Koop, Competition between water uptake and ice nucleation by glassy organic aerosol particles. *Atmos. Chem. Phys.* **14**, 12513–12531 (2014).
104. C. Wong, D. Vite, S. A. Nizkorodov, Stability of α-pinene and d-limonene ozonolysis secondary organic aerosol compounds toward hydrolysis and hydration. *ACS Earth Space Chem.* **5**, 2555–2564 (2021).
105. N. R. Smith *et al.*, Viscosity and liquid–liquid phase separation in healthy and stressed plant SOA. *Environ. Sci. Atmos.* **1**, 140–153 (2021).
106. J. W. Grayson, M. Song, M. Sellier, A. K. Bertram, Validation of the poke-flow technique combined with simulations of fluid flow for determining viscosities in samples with small volumes and high viscosities. *Atmos. Meas. Tech.* **8**, 2463–2472 (2015).